

Freefall movement decomposition of a payload released by aircraft: study of aerodynamic coefficients using the LS-DYNA ICFD solver

Charlotte MICHEL¹, Edith GRIPPON¹, Mathieu SEULIN¹, Vincent LAPOUJADE¹

¹DynaS+, 5 avenue Didier Daurat 31400 TOULOUSE France

Abstract

Through its multi-physics aspect, the airdrop domain is chosen to demonstrate the new FSI capacities recently developed within the LS-DYNA software (more specifically using the ICFD solver). To do this, DynaS+, French, Spanish and Portuguese distributor of LS-DYNA and associated services got a research and innovative subvention from the French Government, RAPID financing.

The main goal of this project, PARAFU, is to succeed in modelling the complete sequence of an airdrop, which includes three main phases:

- i. the payload freefall,*
- ii. the deployment of the hemispherical parachute,*
- iii. and the gliding phase when the payload is supported by the parachute sail.*

Each step includes aerodynamic and fluid-structure interactions problems more or less complex. This paper focuses on the payload freefall phase modelling.

The falling movement of the payload released by the aircraft has been decomposed into simple motions. The package undergoes translation, rotation and combination of both, for Reynolds numbers ranging from 10^4 to 10^6 . Similar cases from the literature have been reproduced in order to validate the ICFD solver capabilities. The aim is to evaluate its accuracy in reproducing aerodynamic phenomena such as drag and lift observed in these configurations.

Particular attention has been paid in order to optimize the associated calculation times. Different models of turbulence have been studied.

1 Introduction

The main goal of military airdrops is the accurate delivery of cargo released from a moving air vehicle via parachute. The airdrop trajectory results from the movement of the dropped package and the dynamics of the parachutes deployment (Fig. 1). Although multi-physic modelling is now being used to analyse the flow around inflated parachute canopies [1, 2], very little has been done in the area of payload aerodynamics [3, 4].

The state of affair is made very complicated by the fact that there are many different dynamic regimes characterizing the flows around the parachutes payload during a typical airdrop operation, i.e.:

- i. ramp roll-out and tip-over,*
- ii. freefall prior to and during parachute deployment,*
- iii. descent and landing under a fully inflated canopy [3].*

The package undergoes translation, rotation and combination of both, for Reynolds numbers ranging from 10^4 to 10^6 .

Although LS-DYNA® ICFD solver appears to be a viable proposition in providing detailed fluid physics of the entire airdrop system from first motion in the aircraft until the payload reaches the ground, it must first demonstrate its ability to accurately reproduce elementary aerodynamics phenomena with simple geometric forms.

With this objective in mind and after describing the released package movement (Part 2), the present paper shows, for different wind speeds, what results can be obtained with rectangles of variable slenderness in static (part 4) and dynamic cases (part 5). Two models of turbulence are studied: the Reynolds Averaged Navier Stokes (RANS) one and the Large Eddy Simulation (LES) one. Particular attention has been paid in order to optimize the associated calculation times. In fact, one of the project main goal is to make this technology accessible to SME and companies with limited IT resources.

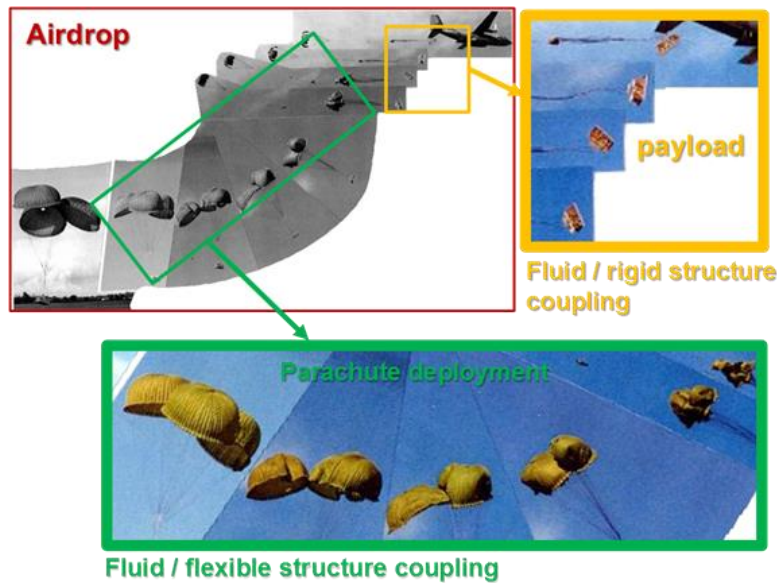


Fig. 1: Highlighting of two types of fluid-structure interactions during airdrop

2 Freefall movement decomposition

2.1 Generalities

The study of dropping payloads seems particularly justified given that many major parachute dysfunctions are associated with the interaction between the package and the parachute during deployment. In addition, some swings observed during flights under canopy have a significant effect on the payload landing angle and therefore on the resulting impact shock.

Nevertheless, experimental measurements of payloads complete behaviour during their fall are still difficult to access. Then, it seems more appropriate to decompose the global movement into several simpler ones for which there are experimental data from wind tunnel test.

2.2 Real case: dimension, velocity, motion and trajectory

2.2.1 Characteristic dimension and motion

During airdrop, the released payloads have variable sizes, shapes and masses: ranging from a truck to a paratrooper. In our study, we focus on a typical rectangular payload with a characteristic dimension of 1m.

For this type of package, three main phases are observed:

- i. Tip-over during ramp exit,
- ii. Spinning during parachute deployment,
- iii. Descent with a certain angle of incidence under fully inflated canopy.

During these three phases, the characteristic movements are therefore translations with a certain angle of incidence and coupled movements of translations and dynamic rotation.

2.2.2 Velocity and trajectory

Each phase identified during airdrop is characterised by the payload movement and its associated speed Fig. 2. Three velocity types can be distinguished: horizontal velocity (parallel to the ground), vertical velocity (perpendicular to the ground) and rotation velocity.

The initial horizontal velocity depends on the aircraft speed. Once the package exited, the velocity decreases almost linearly until the parachute deployment, then reaching an average speed of 5m/s.

The vertical speed largely depends on the drop height and the payload mass. The initial free fall acceleration phase is followed by a deceleration one during the parachute deployment. Once fully deployed, the package finally reaches a constant speed until landing.

During the phases 1 and 2, the rotation speed is on average equal to plus or minus $\pi/2$ per second. During flight under canopy, an oscillation phenomenon is also observed, but is neglected in our study. Table 1 summarizes the average values of released payloads vertical, horizontal and rotational speeds.

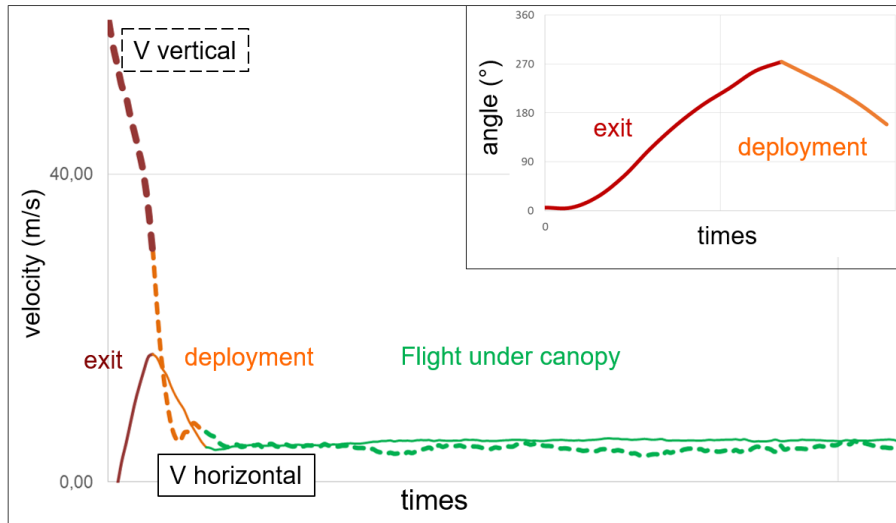


Fig.2: Horizontal & vertical speeds and angle of rotation during the three airdrop phases

	exit	deployment	flight under canopy
V horizontal	40 m/s	10 m/s	5 m/s
V vertical	5 m/s	5 m/s	5 m/s
V rotation	$\pi/2 \text{ s}^{-1}$	$-\pi/2 \text{ s}^{-1}$	Constant angles

Table 1: Horizontal and vertical velocities (V) during the three airdrop phases

2.3 Studies cases

The study of a 1m characteristic length package real behaviour has enabled to distinguish several drop phases with speeds equal to 40, 10 and 5 m/s (corresponding respectively to Reynolds Re equal to 2.8×10^6 , 6.9×10^5 and 3.4×10^5).

Taking into account this previous information, different literature cases with experimental data have been chosen according to their relevance. In a test lab, a translation movement corresponds to a fixed object in an air flow.

2.3.1 Static decomposition: translation with a fixed angle

For static analyses, five cases have been chosen among the ones described by R.D. Blevins [5]. A detailed description of each case is available in this reference. The objective is to numerically retrieve the same flow types and drag results for:

- A 2D rectangle with increasing lengths and a 2D rectangle with varying corners shapes, for Reynolds higher than 10^4 (Fig. 3),
- A 2D square with increasing tilt angles, for a Reynolds of 4.7×10^4 (Fig.4),
- A 3D rectangle with increasing lengths, for a Reynolds of 1.7×10^5 (Fig. 5),
- A 3D cube and a 3D rectangle for a Reynolds superior to 5×10^5 (Fig. 6),
- A 3D thin plate with increasing tilt angles, for a Reynolds higher than 10^4 (Fig. 7).

Although some of these cases are known to be Reynolds-independent, some publications do not give exactly the same drag values for Reynolds between 10^4 and 10^6 (P. Martinez-Vazquez [16] for the Fig. 7 case). In the literature, very few static cases have been studied for Reynolds superior to 5×10^5 .

The last 3D case (Fig. 7) is also studied dynamically. Then it will be possible to quantify the associated dynamic effects.

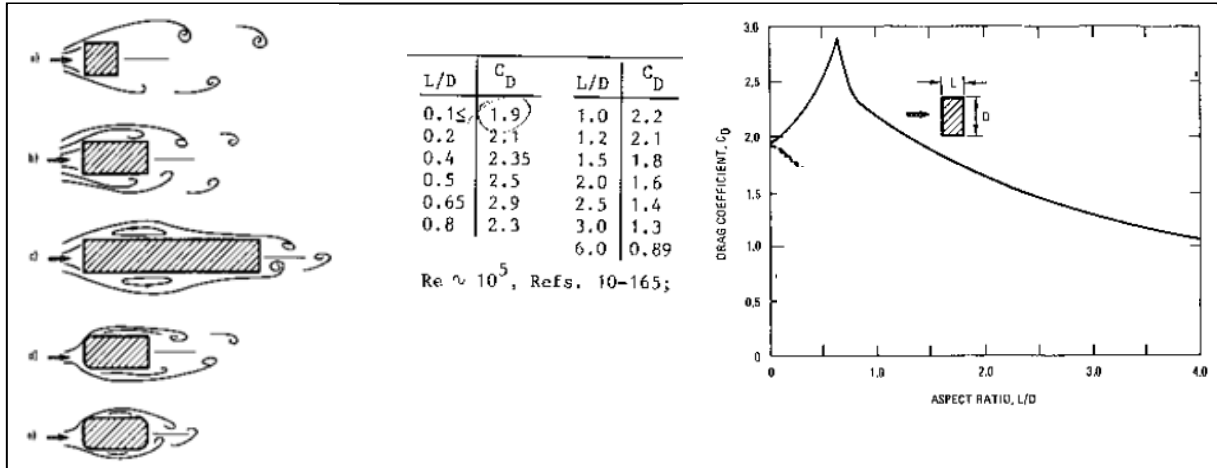


Fig. 3: Drag of two-dimensional bluff section: Effect of length and shape - $Re > 10^4$

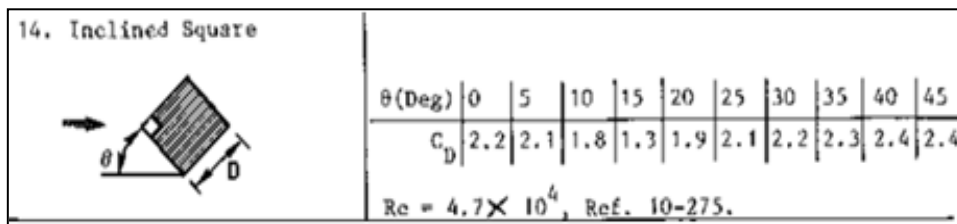


Fig. 4: Drag of two-dimensional bluff section: Inclined square – $Re = 4.7 \times 10^4$

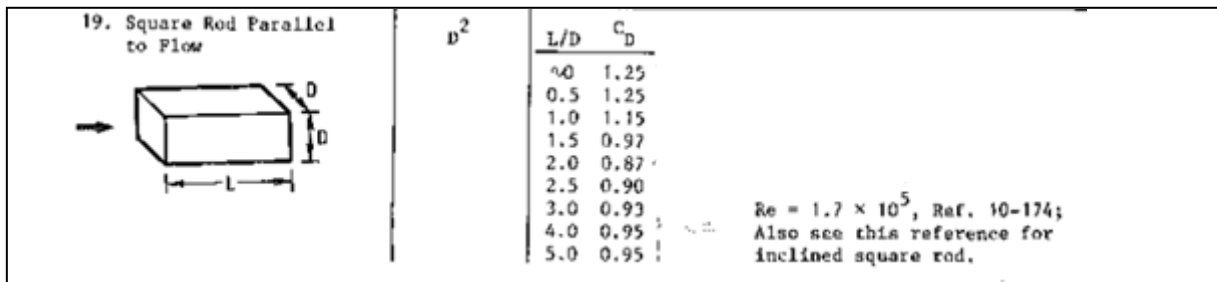


Fig. 5 : Drag of bluff bodies : Effect of length - $Re = 1.7 \times 10^5$

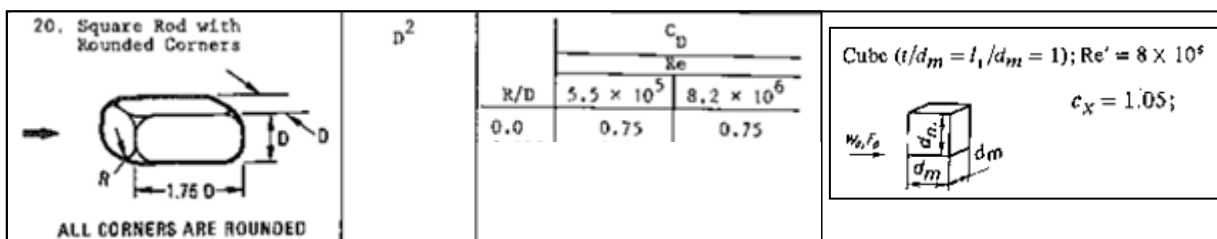


Fig. 6: Drag of bluff bodies : $Re > 5 \times 10^5$

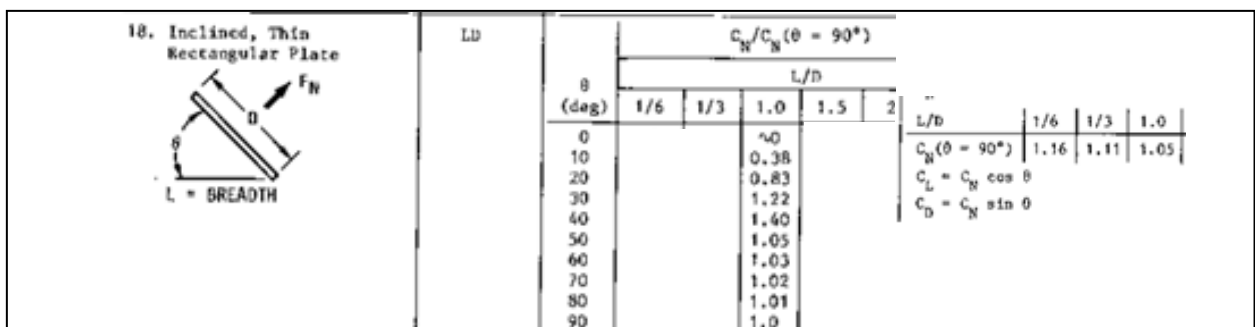


Fig. 7: Drag of bluff bodies : Inclined thin rectangular plate - $Re > 10^4$

2.3.2 Dynamic decomposition: translation with dynamic rotation

The lift and drag estimated from static analyses of a rotated flat plate are different from those taking into account the dynamic nature of the plate motion [6]. This is the reason why a dynamic case from the literature [7] has also been studied in order to validate the use of the ICFD solver in modelling packages in rotation.

This case describes an autorotating square flat plate around a fixed axis (Fig. 8). The test sheet is a piece of expanded polystyrene, 1 m square, 0.0254 m thick and weighing 2.7 kg. The chosen wind velocity is $V=5\text{m/s}$ and the plate rotation velocity is equal to $\pi\text{ s}^{-1}$.

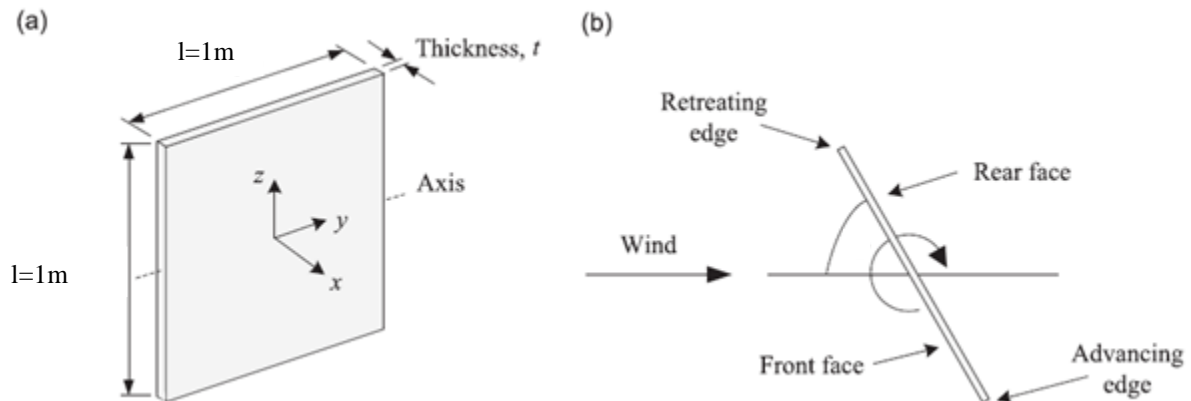


Fig. 8 : (a) Dimensions and orientation of the plate and (b) Nomenclature associated with the autorotating plate

3 Computational details

3.1.1 Common configuration

Every simulation is carried out using the LS-DYNA ICFD solver on a computer cluster and on 28 cores belonging to a single compute node. The computers are Intel Xeon E5 2690 v3.

For the several case studies, one of the objectives is to achieve a computational time of 30 min for 2D simulations and 24 hours for 3D ones. For static analyses, convergence is established either once the pressure fields become periodic or when a virtual particle of fluid gets through the whole domain. The aerodynamic coefficients presented herein are averaged over this period. The lift coefficient, C_l , uses the component of the resultant pressure force perpendicular to the flow and the drag coefficient, C_d , uses the component of the resultant pressure force parallel to the flow.

The ICFD solver uses a two-steps Taylor-Galerkin fractional-step finite element method, which is of second order accuracy [8, 9]. Furthermore, the ICFD solver makes use of powerful automatic mesh generator that will generate the mesh and only leave to the user the responsibility of providing good boundary conditions [10]. The ICFD solver employs an unstructured tetrahedral mesh using special elements to resolve boundary layers, and contains all pre-and post-processing required for CFD analyses.

The boundary conditions considered are the same for all cases:

- An air inlet with a specific defined velocity, an air outlet with a given zero pressure,
- A “non-slip” condition on the object to consider a velocity gradient in the boundary layer and then viscosity, a “free-slip” condition on the side walls.

The air standard characteristics are chosen for the density ($\rho=1.225\text{ kg/m}^3$) and the viscosity ($\mu=1.78e-5\text{ Pa}\cdot\text{s}$). The incoming velocity V varies between 1 m/s, 5 m/s, 10 m/s and 40 m/s, thus covering a wide range of Reynolds numbers based on the body characteristic dimension ($l=1\text{m}$).

Knowing the cases geometry and the Reynolds numbers, Re , the following indications are considered:

- The size of the fluid domain is chosen so that the package is sufficiently far from the boundaries so to avoid edge effects which could have an influence on the lift and drag [11].
- The mesh in the boundary layer depends on the chosen turbulence model and the targeted Y^+ . The boundary layer first element size, dx , is calculated using the flat plate theory [12]. For a RANS model, a minimum of three elements in the boundary layer is recommended and an Y^+

around 30 is generally targeted. For a LES model, around a dozen elements is generally advised (three minimum) with a small Y^+ around 1 [13].

- The time step, dt , is calculated from the model smallest element size and the flow velocity. A scale factor of an order of magnitude is then applied to fasten the computational time. A sensitivity study previously made shown that the time step does not impact the results but can significantly increase the convergence time if it is raised too much.
- The model final time, T , is taken slightly greater than the time necessary for a virtual particle to cross the entire domain. Indeed, without stall or recirculation phenomena, the simulation should then be converged.

The package mesh size could be determined using theory [14]. In our case a 10mm size is chosen.

The static study objective is to find a common model setting to all literature cases, in a minimum optimized time, while still controlling the results accuracy.

3.1.2 *Static and dynamic: Turbulence model choice*

CFD (Computational Fluid Dynamics) approaches are based on the averaged Navier-Stokes equations. Despite significant progress in the unsteady turbulence modelling, as far as we know there still does not exist a universal method enabling to completely model every flow categories occurring during airdrop. Indeed, when the package undergoes high velocity rotations, the presence of a wall, where originates the turbulence then propagating around the object, represents a technological barrier for the CFD approach [15].

RANS modelling, standing for « Reynolds Averaged Navier Stokes », decomposes the movement variables (such as velocity and pressure for an incompressible flow) into their statistic average and this average variation. Since RANS models consider a time averaged version of the governing equations, such models will be more adequate where transient effects are not important and a stationary solution can be reached.

A different approach consists in decomposing the movement depending on the variations scales. This way, the flow large scales are explicitly calculated and the small ones are to be modelled. This LES approach, standing for “Large Eddy Simulation” consist in decomposing the movement variables using a spatial filter. From a numerical point of view the limit is set by the mesh size. The resolved components are still time dependent allowing the analysis of instantaneous quantities even in flows that are stationary in the average. The time iteration is usually mesh size dependent and the model used by the ICFD solver is the classical Smagorinsky model. By its definition, the LES approach is above all three-dimensional.

The ICFD solver offers several turbulence models (Standard k -Epsilon, LES-Smagorinsky, LES-Wale). In its latest release, it also includes some k - ω models as well as the realizable k - ϵ turbulence model which is considered to be an improvement over the standard RANS one [10, 16].

Therefore, the RANS realizable model is chosen for static analyses [11] and the first boundary layer element size is determined in order to maintain a Y^+ to a maximum of 30 for velocities from 1 to 10 m/s. This choice might not be specifically adapted to a 40 m/s speed but is kept in the prospect of a single model setting for all cases. For dynamic analysis, a LES model is chosen.

3.1.3 *Selected numerical configuration*

Considering previously made sensitivity studies, some characteristics have been chosen for the first five static cases and are described Fig. 9. The domain is large enough to include every physical values variation phenomena.

Different velocities are assessed and the velocity considered influences the time step dt and final time choice T (table 2). The 2D cases have between 20 000 and 50 000 elements and run in less than one hour. Except for the plate case, the 3D models have around 4 000 000 elements and run in approximately a day.

The plate, by its special geometry, leads to a smaller model with “only” around 1 500 000 elements. Indeed, being thin, the plate fine mesh area is much smaller than for the packages, which influences the mesh generation. This particularity will be discussed later.

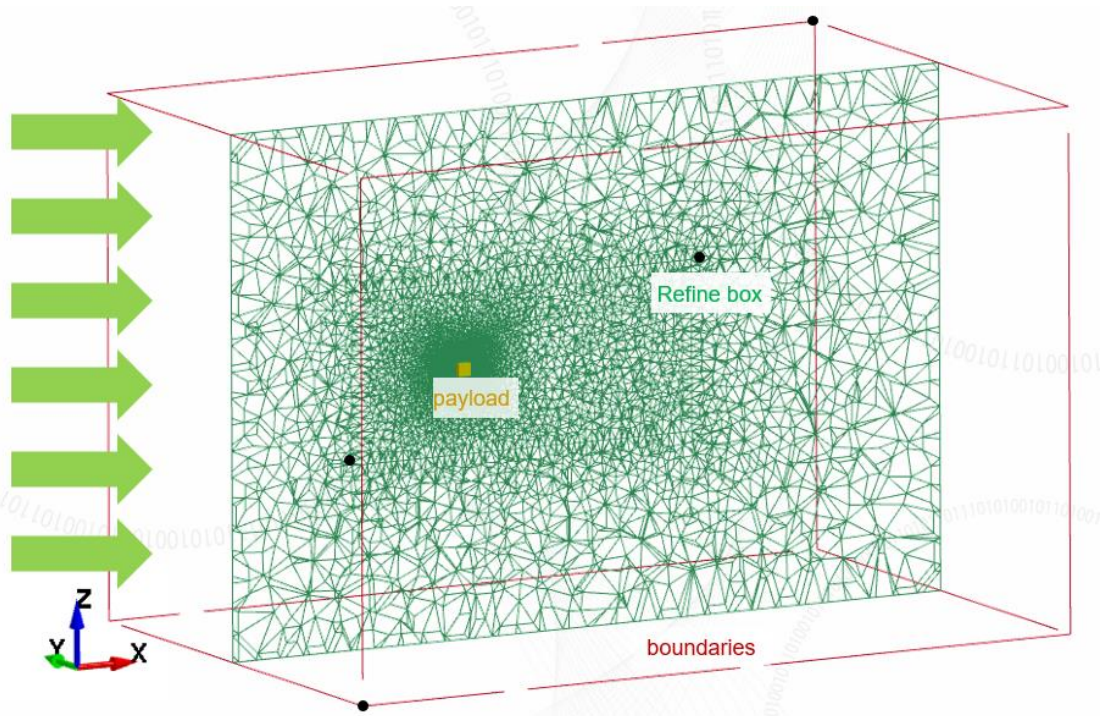


Fig. 9: View of a static model settings: Domain, refinement box and associated mesh

	Computation time	T (s)	Number of elements (k = thousand)
5 m/s in 2D (Fig. 3)	13 à 30 min	12s	20 k to 49 k
10 m/s in 2D (Fig. 3)	30 min à 49 min	12s	20 k to 49 k
1 m/s in 2D (Fig. 4)	10 min	35s	20 k
5 m/s in 3D (Fig. 5)	< 30 h	12s	4 193 k
3D with $Re > 5 \times 10^5$ (Fig. 6)	10m/s: < 30 h	8s	3 841 k
	40m/s: < 30 h	1.5s	3 841 k
5 m/s in 3D (Fig. 7)	5h	10s	1 456 k

Table 2: Summary of the static models main characteristics

For dynamic cases, another domain has been chosen to be in line with the reference publication [17] while also maintaining enough distance between the plate and the boundary conditions (Fig. 10). A later study will enable to quantify this domain choice influence on the numerical results accuracy.

A cylindrical refinement box is used rather than a previously chosen rectangular one. Indeed, it better fits the dynamic behaviour of the rotating plate.

The input velocity is equal to 5 m/s and the rotation velocity is established at π/s via a growing curve getting from 0 to πs^{-1} in 0.1 second. This unsteady model type requires to activate the remeshing option.

Two different boundary layer strategies are tested and these choices have an impact on the mesh size and the total number of elements (table 3):

- i. The first modelling corresponds to a Y^+ around 1 and the boundary layer contains 10 elements which size rapidly increases as their repartition follows a specific growth scale factor.
- ii. In the second modelling, the Y^+ is close to 10 and there are only 3 elements in the boundary layer (also following a growth scale factor repartition).

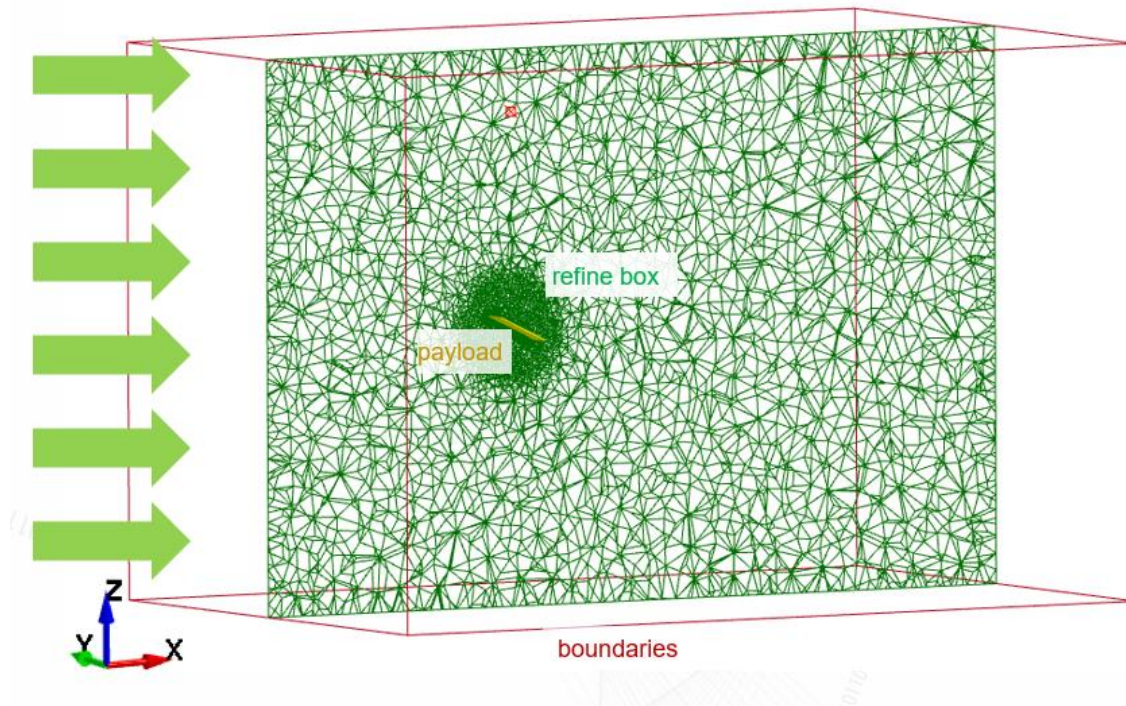


Fig. 10 : View of the dynamic model settings: Domain, refinement box and associated mesh

	Computation time	T	Number of elements (k = thousand)
Plate at 5 m/s – fine boundary layer	<20h	2.5s	2 500 k
Plate at 5 m/s – coarse boundary layer	<3h	2.5s	1 567 k

Table 3: Summary of the dynamic models main characteristics

4 Static Cases using RANS model

4.1 2D Cases

4.1.1 Effect of the package length and shape on the flow patterns for $V=5$ m/s and on the drag results for $V=5$ m/s and $V=10$ m/s

The Fig. 11 shows the superposition of experimental (for $Re \sim 10^5$) and numerical results (for $Re=3.4 \times 10^5$ and 6.9×10^5) for various bluff bodies. Five different lengths have been modelled and analysed. The width D has been kept constant at 1m and the length L has evolved between 1m and 6m. For the $L=3$ m case, three corners' shapes have been tested, from sharp to round (first only on the nose side and then on every corners).

For all configurations, there is a good correlation between experimental and numerical results, and in computation time inferior to 30 minutes. Two effects are underlined:

- i. The drag tends to decrease when the fineness ratio increases. And for these 2D cases, the drag results appear fairly independent from the Reynolds number [5]. Indeed, they are almost identical for two different velocities: 5 and 10 m/s.
- ii. The corners shape significantly influences the drag coefficient which decreases when the corners change from sharp to round.

To study the corners shape effect, a 10mm mesh size was kept along the entire package edge. This might not be the best strategy as the computation time significantly increased when the corners got rounded. A local mesh refinement might fasten the calculation and will be considered for further studies.

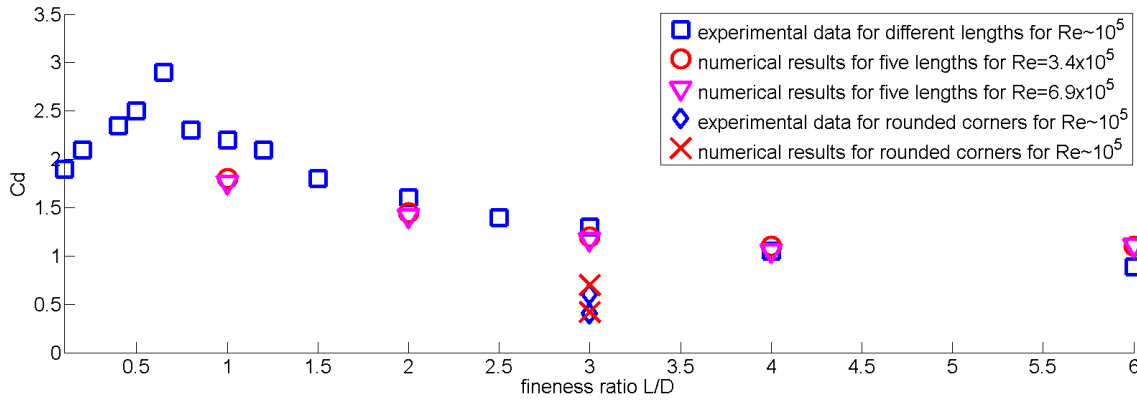


Fig. 11 : Drag coefficient experimental and numerical results for various lengths and shapes bluff bodies. For $L=3m$, from top to bottom, the values respectively correspond to sharp corners, rounded nose section and rounded nose and tail section

The Fig. 12 and Fig. 13 show some cases velocity fringes, depending on the packages length and shape. The flow patterns are similar to the ones described in the corresponding publication [5]. In the first three cases (Fig. 12 (a)) the flow is deflected by the sharp-edged nose and only reattaches for a long enough rectangle. It does not for the square and the 3m rectangle but it does for the 6m rectangle. In this latter case, we can also observe a typical recirculation zone, highlighted in the Fig. 12 (b).

For the $L=3m$ rectangle (Fig. 13), when the front corners are rounded (b), the flow separation is greatly reduced and the flow reattaches. This significantly decreases the resulting drag. Since the rounded nose enables the flow to reattach, to round the rear corners (c) also decreases the drag (otherwise it would have a little effect) and diminishes the wake.

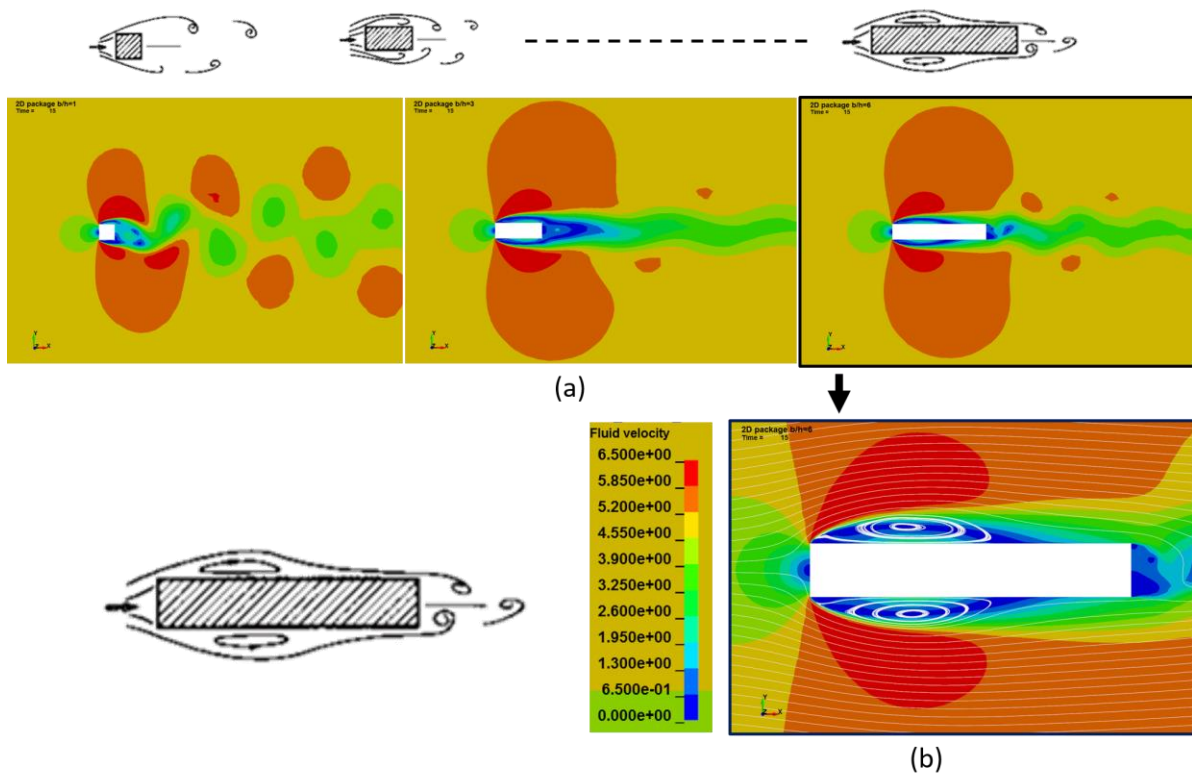


Fig. 12: Fluid velocity fringes for rectangular packages: (a) Lengths 1m, 3m and 6m - (b) Length 6m zoom and streamlines

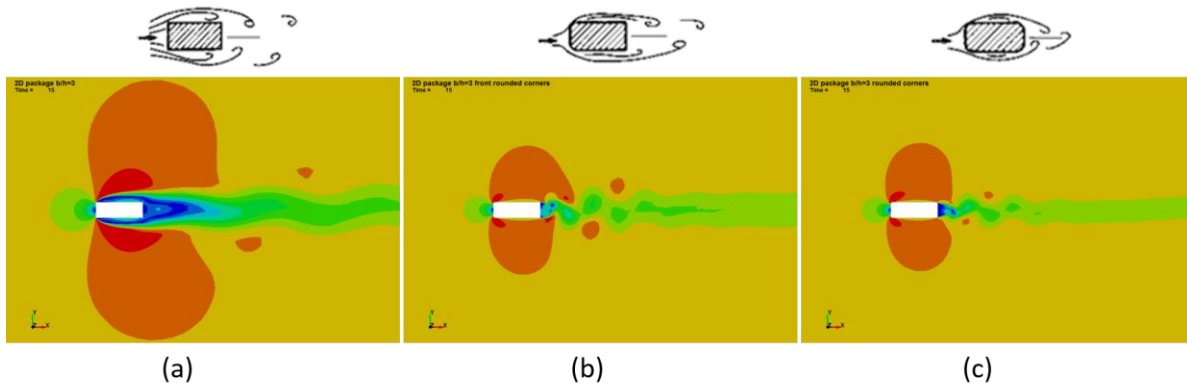


Fig. 13: Fluid velocity fringes for 3m length rectangular packages: (a) sharp edges, (b) rounded nose and (c) four rounded edges

4.1.2 Effect of the package angle on the drag results for $V=1$ m/s

The Fig. 14 (a) shows the superposition of experimental (for $Re=4.7 \times 10^4$) and numerical results (for $Re=6.9 \times 10^4$) for a square with various inclination angle. Globally this 2D case seems rather well modelled, although 15° and 45° angles would merit to be studied more carefully. For each angle, the computation time, approaching 10 minutes, is really competitive. The Fig. 14 (b) shows the final time velocity fringes for a 30° angle.

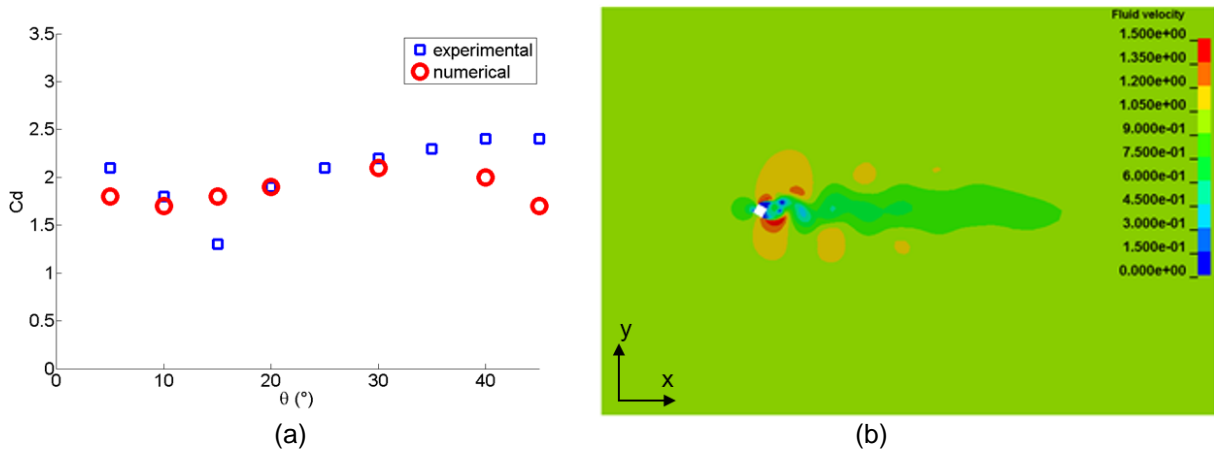


Fig. 14: (a) Drag coefficient experimental and numerical results, (b) fluid velocity for a 30° angle at $t=35s$

4.2 3D cases

4.2.1 Effect of the package length on the drag results for $V=5m/s$

The Fig. 15 shows the superposition of experimental (for $Re = 1.7 \times 10^5$ and $Re > 5 \times 10^5$) and numerical results (for $Re = 3.4 \times 10^5$ and $Re > 5 \times 10^5$) for various bluff bodies. Seven different lengths have been modelled, of which two for different Reynolds numbers. Every result has been obtained in less than 30 hours for models containing around 3.8 million elements.

When the Reynolds is lower than 5×10^5 , numerical models and experimental measures are in good agreement. The variation in the experimental drag data due to the Reynolds growth is also captured numerically. For the 10 m/s and 40 m/s velocities, the correlation between experimental and numerical values is rather good although more instabilities are noticed on the drag results (especially for 40 m/s). This behaviour is not really surprising considering the previously made choice on the boundary layer modelling. In fact, the first element size is too large to theoretically keep Y^+ around 30 for a velocity of 40 m/s. Then, a specific model should rather be used for this higher velocity. Also, considering the dynamic nature of the package airdrop (Fig. 2), it would be good to find in the literature a dynamic case at 40 m/s to study.

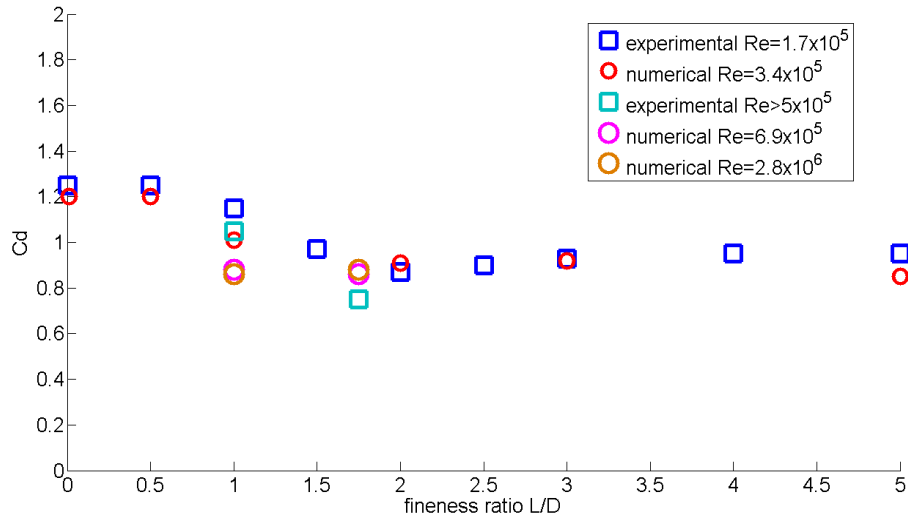


Fig. 15 : Drag coefficient experimental and numerical results

4.2.2 Effect of the thin rectangular plate angle on the drag results for $V=5$ m/s

Two publications [5] and [16] are used to study the thin plate in static analyses. They give different lift and drag results for a 40° angle, corresponding to the stall region, relatively sensitive to the experimental tests conditions [7]. For the other angles the small difference between both curves can be explained by the $\pm 5\%$ measurement precision.

The Fig. 16 shows the superposition of experimental (for these two publications) and numerical results in static for a thin rectangular plate. Globally, the numerical results correlate well with the experimental data. Regarding the lift, almost every numerical point lies within the two curves corridor. Regarding the drag, the numerical results tend to slightly overestimate the experimental data.

This small gap might be explained by the specific thin plate geometry leading to a special mesh generation. In fact, as previously noticed, as the plate is a thin object there are much less elements in this model than in the rectangle package ones. The zones with strong mesh size gradient might not be sufficiently finely meshed. However having less elements also leads to much faster calculations. Indeed the computation time drops to 5 hours compared to 30 hours for the previous 3D package models (Table 2).

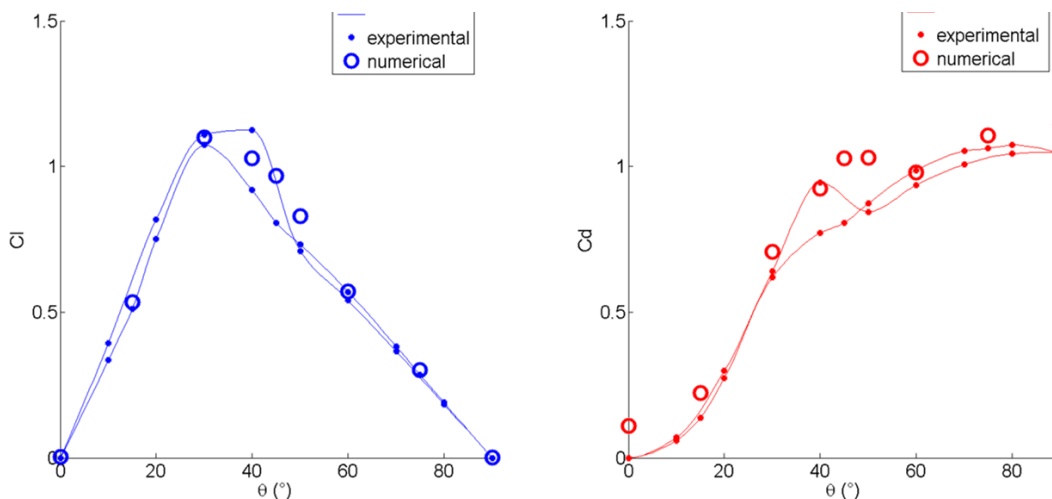


Figure 16. Static lift and drag coefficients for $V=5$ m/s. For experimental data, the accuracy is approximately $\pm 5\%$

The plate mesh particularity will be studied in details in a further work. Indeed, this plate case is especially interesting as its thin characteristic enables to model it by either solid or shell elements. Both these possibilities will be considered and compared. The drawn conclusions will then be used when finally modelling the parachutes, by definition meshed with shell elements.

5 Dynamic case using LES model

The plate is allowed to spin freely around its centre of gravity and is located near the centre of a wind tunnel with a free stream velocity of 5 m/s [17, 18].

The presented results come from a first feasibility study showing the ICFD solver efficiently in modelling dynamic analyses. A second study will later enable to optimize these calculations in term of computation time and accuracy.

Here two parameters only have been tested: the first boundary layer element size, dx , and the total number of elements in this same layer. The corresponding choices are illustrated in Fig. 17.

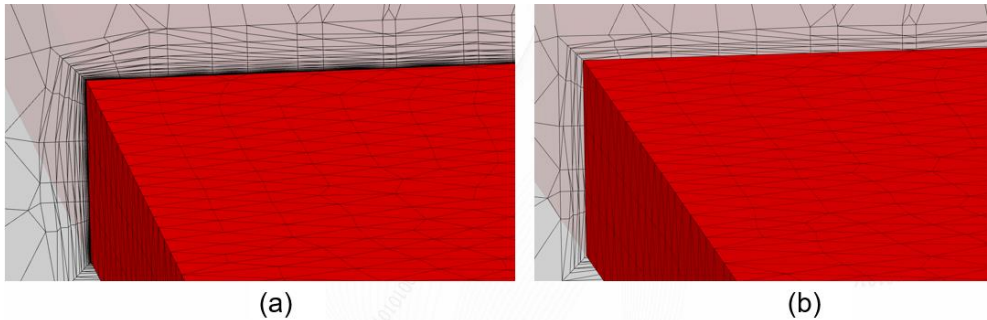


Fig. 17. View of the boundary layer for (a) $Y+=1$ and (b) $Y+>10$

The experimental data come from the tests performed by Martinez-Vazquez et al. [16] in the wind tunnel at the University of Auckland. The numerical values are obtained from a model respecting the Fig.10 configuration.

Fig. 18 shows the instantaneous velocity fringes in the middle section plane for different angles of rotation and $Y+>10$ (the plots are similar when $Y+=1$). Leading and trailing edges vortices can be observed in the wake of the autorotating plate. The vortex created behind the plate starts to detach after a 90° angle (as kicked out by the plate). The velocity drop observed below the plate slightly after 180° is due to the confrontation between the incoming flow and the fluid driven by the rotating plate and so going in the opposite direction. After the first plate half rotation, we can see significant fluid structure interactions.

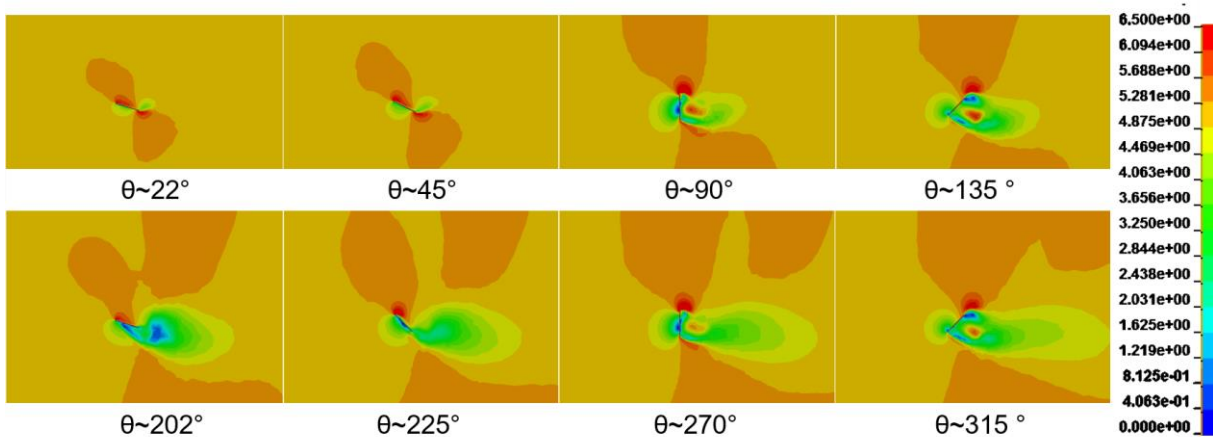


Fig. 18 : Fluid velocity fringes for $Y+>11$

The differences between the Fig. 18 top and bottom fringes are due to the progressive establishment of the dynamic phenomena specific to the autorotation. Here, the experimental values are averaged on 120s (corresponding to a large number of cycles) whereas the numerical data only correspond to one cycle (Fig. 19). However, numerical results for the lift and drag coefficients show close resemblance to experimental values (Fig. 19).

The two models give really similar results but the one considering a $Y+$ slightly over 10 is seven times faster. The oscillations observed on the numerical curves come from the remeshing steps.

The lift is globally over-estimated whereas the drag magnitude correlates really well with the experiments. This accuracy difference might come from the fact that the flow direction induces higher pressure forces in the drag direction than in the lift one. The lift is more influenced by the viscosity, highly dependent on the boundary layer modelling choices. Drag values are accurately predicted despite a small phase offset. These results are really encouraging.

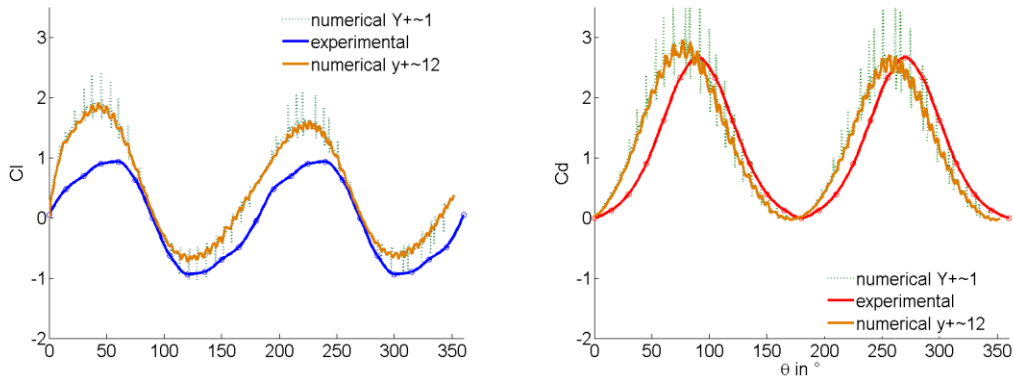


Fig. 19.: Lift and drag coefficients versus rotation angle – Numerical (LES) and experimental results

6 Conclusion

As part of a global project in charge of modelling the complete sequence of an airdrop, the work presented in this paper focuses on the payload modelling. The cases presented are representative of the problems addressed during a package airdrop. While being simple they allow to underline the ICFD solver performance. The numerical results confirm the solver capacity in modelling this type of fluid-structure interactions (FSI), while maintaining acceptable computation times.

For static analyses, a single optimized model was used to run all the 2D and 3D bibliography cases. The numerical results were assessed looking at both the aerodynamic coefficients (especially the drag) and the plot fringes. Globally, a good correlation has been obtained between numerical and experimental results.

In dynamic, a complex fluid-structure of an autorotating flat plate was simulated. The numerical results agree reasonably well with the experimental data when looking at the aerodynamic coefficients at the plate's surface. One next step is to apply similar modelling techniques to the autorotation of a real payload.

Static and dynamic simulations have been run using two different turbulence models: RANS and LES respectively. The several airdrop phases combine static and dynamic behaviours. Since one of the project objective is to model the complete airdrop in a single run, further studies will assess the LES model on static applications.

The final step will be to use this ICFD solver in the case of flexible structures, representative of parachutes, in order to make full use of the Powerful FSI capabilities of LS-DYNA.

7 Acknowledgements

DGA TA is acknowledged for providing airdrop experimental data and some of the bibliography cases.

Iñaki Çaldichoury, Facundo Del Pin and Rodrigo Diaz are acknowledged for the help and precious advices they gave during this study.

This work was realized as part of a RAPID project financed by the French Government in order to improve parachutes simulation with LS-DYNA.

8 Literature

- [1] Coquet Y., Bordenave P., Capmas G., Espinosa C., "Improvements in fluid structure interaction simulation of parachute using LS-DYNA", 21st AIAA, 2011-2590.
- [2] Tutt B., Charles R. D., Roland S., Noetscher G., "Development of parachute simulation techniques in LS-DYNA", 11th International LS-DYNA Users Conference, 2012.
- [3] McQuilling M., Potvin J., Riley J., "Simulating the Flows About Cargo Containers Used During Parachute Airdrop Operations", 28th AIAA Applied Aerodynamics Conference, Chicago, IL, June 28 - July 1, 2010
- [4] Desabrais K. J., "Aerodynamic Forces on an Airdrop Platform", 18th AIAA, 2005-1634.
- [5] Blevins R.D., "Applied fluid dynamics handbook", Chapter 10, Fluid Dynamic Drag, 1984
- [6] Kenneth J. Desabrais, "Aerodynamic Forces on an Airdrop Platform", 18th AIAA Aerodynamic Decelerator Systems Technology Conference and Seminar AIAA 2005
- [7] Hargreaves D.M., Kakimpa B., Owen J.S., "The computational fluid dynamics modelling of the autorotation of square, flat plates", journal of Fluids and Structures 46 (2014) 111–133
- [8] Codina, R. "Pressure Stability in Fractional Step Finite Element Methods for Incompressible Flows." Journal of Computational Physics 170, no. 1 (2001): 112-140.
- [9] Del Pin, F., Çaldichoury, I. and Paz, R. "LS-DYNA ICFD Theory Manual LSTC", 2011.
- [10] Çaldichoury I., Del Pin F., Paz R., "Latest developments in Automotive Aerodynamics using LS-DYNA®", 14th International LS-DYNA Users Conference
- [11] Perin B., Verdrel O., Bordenave P., Gripon E., Lapoujade V., Belloc H., Caldichoury I., "Computational Fluid Dynamic of NACA0012 with LS-DYNA® (ALE & ICFD) and Wind Tunnel Tests", 14th International LS-DYNA Users Conference
- [12] <http://www.pointwise.com/yplus/>
- [13] Caldichoury I., Del Pin F., Paz R., "Introduction tot he ICFD solver", LSTC training class, 2016
- [14] Gerardo F., Nigro N., Storti M., and D'Elia J.. "Numerical Simulation of the Flow around the Ahmed Vehicle Model." Centro Internacional de Metodos Computacionales en Ingenieria (CIMEC), n.d.
- [15] Martinat G., « Analyse physique et modélisation d'écoulements instationnaires turbulents autour de profils oscillants et d'éoliennes », thesis, Institut national polytechnique de toulouse, 2007
- [16] Shih, T.H, Liou W.W., Shabbir A., Yang Z., and Zhu.J. "A New k-ε Eddy Viscosity Model for High Reynolds Number Turbulent Flows—Model Development and Validation." Computers Fluids 24 (1995): 227-238.
- [17] Coronado Domenge P. X., Velez C. A., Das T., "Large-eddy simulations of an autorotating square flat plate", Applied Mathematical Modelling 0 0 0 (2016) 1–12
- [18] Martinez-Vazquez P., Baker C.J., Sterling M., Quinn A.D., Richards P.J., the flight of wind borne debris: an experimental, analytical, and numerical investigation. Part ii (experimental work), The Seventh Asia-Pacific Conference on Wind Engineering, November 8-12, 2009, Taipei, Taiwan